ASME Journal of Vibration and Acoustics
Online journal at:
https://asmedigitalcollection.asme.org/vibrationacoustics

Greco Moraga
Centre for Industrial Diagnosis and Fluid Dynamics (CDIF), Polytechnic University of Catalonia, Barcelona 08028, Spain
e-mail: greco.alonso.moraga@upc.edu

David Valentín
Centre for Industrial Diagnosis and Fluid Dynamics (CDIF), Polytechnic University of Catalonia, Barcelona 08028, Spain
e-mail: david.valentin@upc.edu

Xiang Xia
Centre for Industrial Diagnosis and Fluid Dynamics (CDIF), Polytechnic University of Catalonia, Barcelona 08028, Spain
e-mail: xiang.xia@upc.edu

Mònica Egusquiza
Centre for Industrial Diagnosis and Fluid Dynamics (CDIF), Polytechnic University of Catalonia, Barcelona 08028, Spain
e-mail: monica.egusquiza@upc.edu

Víctor Fernández
Centre for Industrial Diagnosis and Fluid Dynamics (CDIF), Polytechnic University of Catalonia, Barcelona 08028, Spain
e-mail: victor.manuel.fernandez@upc.edu

Alexandre Presas[1]
Centre for Industrial Diagnosis and Fluid Dynamics (CDIF), Polytechnic University of Catalonia, Campus Diagonal Sud, Building PI (Pavelló I). Av. Diagonal, 647, Barcelona 08028, Spain
e-mail: alexandre.presas@upc.edu

A Time-Domain Demodulation Approach for Extracting Natural Frequencies and Standing-Wave Mode Shapes in Non-Axisymmetric Turbomachinery Components

Measuring the natural frequencies and mode shapes of rotating turbomachinery components under real-operating conditions is particularly important to prevent dangerous operating scenarios. However, this task becomes particularly challenging for runners and impellers because they are rotating, confined, and, in hydraulic turbomachinery, submerged. Furthermore, many existing measurement techniques rely on frequency-domain analysis, where measurements taken from the stationary frame can produce complex spectral responses that complicate interpretation. To address these challenges, this work proposes a method to extract excited mode shapes and their associated vibration frequencies directly from time-domain signals. Mode shapes are recovered through demodulation of the structural response measured once the system reaches a resonant state. Measurements are performed using a laser Doppler vibrometer (LDV) in the stationary frame. To validate the method, a simplified model representing an axial turbomachinery impeller or runner is studied both experimentally and numerically. First, modal analyses under stationary (non-rotating) conditions are conducted to identify the natural frequencies and mode shapes. The structure is then set into rotation and brought to resonance using a piezoelectric actuator, with response measured by the LDV in the stationary frame and by an accelerometer installed in the rotating frame. The proposed method demonstrates the feasibility of accurately extracting mode shapes in complex rotating systems and provides valuable insights for resonance detection and monitoring of such structures. Limitations and potential applications of the methodology are also discussed. [DOI: 10.1115/1.4071343]

Keywords: laser Doppler vibrometry, mode shapes measuring, time-domain analysis, vibration measurements, turbomachinery monitoring, machinery and structural damage identification, mechanical signatures, modal analysis, structural acoustics

1 Introduction

Although turbomachinery is designed to operate under specific conditions, its actual operation often deviates from these on-design conditions due to operational requirements or issues during operation [1–5]. During off-design operation conditions or transient events, several phenomena can occur, leading to the excitation of critical structures, such as impellers and runners. In most severe cases, a structural resonance can be triggered [6–9], leading to mechanical failures due to fatigue [10–18]. In order to prevent these failures, the development of robust measurement and monitoring techniques is highly important for assessing the modal parameters of critical rotating structures and preventing failures. However, these critical structures are rotating and enclosed, and the harsh conditions inside their casing, most of the time, can make direct measurement from the structure extremely challenging. Optical techniques, which do not require direct contact with the structure, remain a promising tool for the vibration monitoring of impellers in turbomachinery systems. Laser Doppler vibrometers (LDVs), in particular, offer the advantage of measuring

[1]Corresponding author.

Contributed by the Technical Committee on Vibration and Sound of ASME for publication in the Journal of Vibration and Acoustics. Manuscript received November 4, 2025; final manuscript received February 20, 2026; published online March 25, 2026. Assoc. Editor: Mostafa Nouh.

 Copyright © 2026 by ASME

from the stationary frame and requiring only a small spot for measurement, making them noninvasive for the structure. Over the past few decades, significant advancements have been made in optical measurement techniques for determining the modal parameters of both stationary and rotating structures. To scan and assess structural modal parameters of stationary structures, laser Doppler vibrometry and photogrammetry have been widely employed [19]. Sriram et al. [20] demonstrated the feasibility of measuring mode shapes and natural frequencies by dynamically gathering data from multiple locations using an oscillating mirror with an LDV. Later, Stanbridge and Ewins [21] proposed the continuous scanning laser Doppler vibrometry (SLDV). By means of continuous circular and straight scan lines, the structural response of a plate was determined within its whole area. Using the frequency response of the plate, the mode shapes were assessed. In the same line, Stanbridge et al. [22] performed an analysis by moving an LDV in straight and circular paths on a cantilever plate to determine mode shapes from the natural frequency sidebands. Further advancements were made by La et al. [23], who proposed a two-dimensional continuous sinusoidal scanning technique for plates combined with a Chebyshev series formulation to analyze vibration mode shapes, achieving good agreement between experimental and numerical results. This methodology was implemented later by Stanbridge et al. [24] on a cantilever plate, evaluating factors like structural continuity, speckle noise, scan frequency, and limitations when scanning curved surfaces. These studies illustrate the progression of LDV techniques, which have become increasingly sophisticated for capturing mode shapes in stationary structures, greatly enhancing operational modal analysis and even damage detection [25].

For rotating structures, measuring modal parameters is more complex due to the distinct stationary and rotating reference frames. Presas et al. [26] explained the additional challenges posed by rotating measurements, particularly regarding measurement location and rotation speed. Few authors have attempted to measure modal parameters in rotating structures using LDV. For instance, Stanbridge et al. [27,28] and Halkon and Rothberg [29] investigated various techniques for performing LDV scanning on rotating disks and bladed-disk (BD) structures, including the use of rotating mirrors and circular scanning methods. They also analyzed the LDV response in the frequency domain using the obtained Fourier coefficients, and discussed technical limitations and the influence of factors such as the alignment between the structural and LDV measurement axes, the positioning of the mirrors, and speckle noise at high rotational speeds. In the analysis of bladed structures in air, Gasparoni et al. [30] performed a modal analysis of a rotating fan using tracking SLDV. In that study, each blade was scanned at different rotational speeds using a cloverleaf pattern, which captured the fan bending response under operational conditions excited by impacts. For submerged bladed structures, on the other hand, Castellini and Santolini [31] mapped the vibration levels of an operating naval propeller in water using a tracking laser vibrometer, identifying the main mode shapes excited during operation. Abbas et al. [32] measured the natural frequencies of a submerged, rotating propeller by tracking a single point on the blade, using a set of mirrors to redirect the LDV beam. Although the vibration mode shape was not determined experimentally in that study, it was possible to determine the natural frequencies of the propeller while rotating. The results shown in Refs. [31,32] indicate that the natural frequencies of the propeller do not split due to rotation, contrary to the effects observed in submerged rotating disks [33,34], however, no further analysis is provided on the matter. Lyu et al. [35–37], on the other hand, were able to determine the natural frequencies and mode shapes of a three-bladed rotating structure under random excitation. Using a controlled mirror system, the LDV scanned the motion of the blade along a one-dimensional path. The LDV was assisted by a camera to detect the blade limits. This enabled successful blade tracking and the assessment of natural frequencies and mode shapes, which showed good agreement with numerical predictions. Notably, in the above-mentioned studies [27–32,35–37], there was a considerable distance between the measured structure and the sensor, making it possible to carry out a measurement of the structure by tracking a point and scanning continuously from different trajectories. This could present a limitation if the goal was to measure the modal parameters of an enclosed rotating structure, such as an impeller. In this context, Presas et al. [38] studied the modal parameters of a rotating disk-blades-disk (DBD) structure within a stationary casing. Measurements were taken in both the rotating and stationary frames using accelerometers and an LDV, respectively. The LDV was fixed in space to scan the periphery of the disk-like structure. Although mode shapes were not extracted by scanning the entire surface, a thorough analysis of the natural frequency sidebands was conducted to characterize the diametrical mode shapes of the structure in the frequency domain, correlating measurements from both reference frames.

Considering the challenges associated with measuring modal parameters directly from a rotating machine in operation, the ability to identify and monitor the excitation of specific mode shapes becomes highly important [39,40]. Non-contact monitoring techniques enable real-time insight into the dynamic state of rotating critical structures, allowing for adjustments to operating conditions that can reduce damage and prevent potential failures. In this study, a methodology to determine standing mode shapes of rotating structures and their respective resonance frequencies from the stationary reference frame is proposed. In contrast to previous studies, the present work extends the measurement of mode shapes and resonant frequencies to enclosed rotating structures. It overcomes the limitations associated with direct measurements on rotating structures and the challenges of the interpretation in the frequency-domain sideband analysis by extracting these modal parameters from the time-domain structural response acquired in the stationary reference frame. To carry out this study, the mode shapes and vibration frequencies of various rotating structures are measured from both stationary and rotating frames while the structure is in rotation and under a resonant state. An accelerometer placed on the rotating structure and an LDV fixed on the stationary frame are used for this purpose. LDV measurements are taken through a simulated casing opening, enabling the extraction of mode shapes from the periphery of the structure.

2 Theoretical Background

2.1 Standing Mode Shapes. A standing wave arises when two traveling waves of equal amplitude and frequency interfere while moving in opposite directions. Their energies combine to create a stable oscillating wave, fixed in space. For vibrating structures, these standing waves can be seen in their vibration mode shapes. For a disk-like structure, for instance, standing-wave mode shapes are characterized by the distribution and number of nodal lines (zones with no displacement in blue in Fig. 1) and are dependent on the geometry of the structure and the boundary conditions imposed on it. For a free disk, the mode shapes (n,s) dominated by the out-of-plane deformation of the structure are commonly classified by the number of nodal diameters "n" and circles "s" (see Fig. 1).

The displacement of the disk in the axial direction (out-of-plane) can be written as a function of its geometrical features, material properties, time, and vibration parameters, such as the vibration mode shape and frequency [41]

$$w(r,\theta,t) = \psi(r)\cos(n\theta)\cos(\omega t) \tag{1}$$

with

$$\psi(r) = (A_n J_n(k_{ns} r) + C_n I_n(k_{ns} r)) \tag{2}$$

where w is the displacement, r is the radial coordinate, θ is the angular coordinate, t is the time, J_n is the first-order Bessel

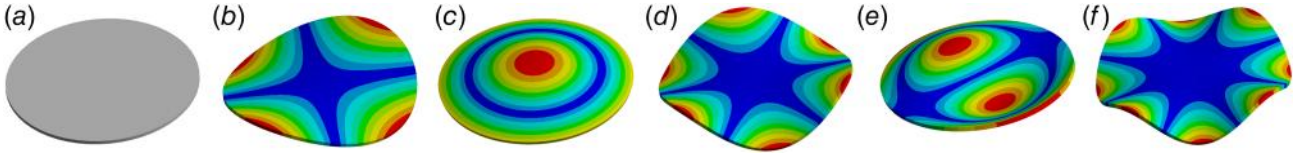

Fig. 1 Free disk and its first mode shapes: (*a*) still disk, (*b*) (2,0), (*c*) (0,1), (*d*) (3,0), (*e*) (1,1), and (*f*) (4,0)

function, I_n is the first-order modified Bessel functions, A_n and C_n are constants determined by the boundary conditions imposed on the disk, ω is the natural frequency of the disk in vacuum, and k_{ns} is a frequency parameter determined by

$$k_{\text{ns}}^4 = \frac{\rho_D h \omega_v^2}{D} \tag{3}$$

with

$$D = \frac{Eh^3}{12(1-\nu^2)} \tag{4}$$

where ρ_D is the disk density, h is the thickness of the disk, E is the Young modulus, and ν is the Poisson modulus.

From this point forward, disk-like structures will be used as examples to explain the methodologies and procedures used in this work.

2.2 Analysis of Vibrating Structures in Rotation. The analysis of a rotating structure can be approached from two frames of reference: the stationary and the rotating frames. To illustrate this idea, let us consider a disk, with radius R, vibrating at a diametrical mode shape $(n,0)$ with a frequency ω, rad/s, and rotating with an angular coordinate θ at a speed of Ω, rad/s relative to the stationary frame. In this case, the rotating frame is attached to the disk, and the Z-axis is shared by both the stationary and rotating frames, as shown in Fig. 2.

If the deformation of the disk is considered only in the Z direction, the displacement in every point of the disk can be obtained, as shown in Eq. (1). However, since the mode shape is diametrical, this analysis can be simplified by studying just the periphery of the disk. Therefore, the function $\psi(r)$ can be considered as a constant by choosing the radial coordinate equal to the radius of the disk R. Then, Eq. (1) can be written as

$$\begin{aligned} w_r(\theta, t) &= \psi(R)\cos(n\theta)\cos(\omega t) \\ &= A\cos(n\theta)\cos(2\pi f_r t) \end{aligned} \tag{5}$$

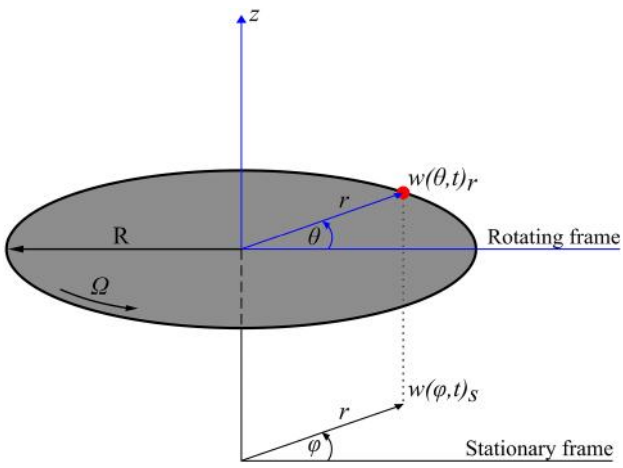

Fig. 2 Rotating and stationary frames of reference

where A is the vibration amplitude at the periphery of the disk, and f_r is the vibration frequency from the rotating frame point of view.

To study the displacement of Eq. (5) from the stationary frame, the rotating frame angular coordinate has to be converted into a stationary frame angular coordinate. This conversion is given by the following expression [34]:

$$\varphi = \theta + \Omega t \tag{6}$$

Then, replacing Eq. (6) in Eq. (5), the displacement in the periphery of the disk from the stationary frame can be expressed as

$$w_s(\varphi, t) = A\cos(n(\varphi - \Omega t))\cos(2\pi f_r t) \tag{7}$$

which can also be written as

$$\begin{aligned} w_s(t) = &\frac{A}{2}\cos(2\pi(f_r - n\Omega)t + n\varphi) \\ &+ \frac{A}{2}\cos(2\pi(f_r + n\Omega)t - n\varphi) \end{aligned} \tag{8}$$

From Eq. (8), two vibration frequencies can be seen from the stationary reference frame

$$f_{1-s} = f_r - n\Omega \tag{9}$$

and

$$f_{2-s} = f_r + n\Omega \tag{10}$$

A contrast between both stationary and rotating frames can be graphically done. For this, let us analyze the red point in Fig. 2. If Eq. (5) is plotted over one revolution of the disk, the time-domain signal obtained from the rotating frame is a pure cosine oscillation, as shown in Fig. 3(*a*), and its frequency spectrum has only one component corresponding to ω_r, as shown in Fig. 3(*b*). Conversely, if Eq. (7) is plotted over one revolution of the disk, the time-domain signal obtained from the stationary frame is an amplitude-modulated (AM) signal, as shown in Fig. 3(*c*). This AM signal is composed of a cosine oscillation due to the disk vibration and a modulation in amplitude corresponding to the diametrical mode shape of the disk while it is rotating with respect to the stationary frame. For this case, the frequency spectrum of the AM signal exhibits two components with half of the amplitude obtained from the rotating frame (as shown in Eq. (8)) and frequencies f_{1-s} and f_{2-s}, as shown in Fig. 3(*d*).

2.3 Demodulation of the Response Signal. As previously mentioned, the vibration signal obtained from the stationary frame is modulated in amplitude by the mode shape of the rotating structure while vibrating in resonance, as shown in Fig. 3(*c*). Therefore, the extraction of the mode shape from a vibrating and rotating structure from the stationary frame of reference is investigated by means of the demodulation of the AM signal $w_s(t)$.

To demodulate $w_s(t)$ from the vibration frequency ω_r, first, the demodulation $v(t)$ is defined as the multiplication of the AM signal by the time function of the vibration, such that considering the phase shift $n\varphi = 0$

$$v(t) = w_s(t) * \cos(2\pi f_r t) \tag{11}$$

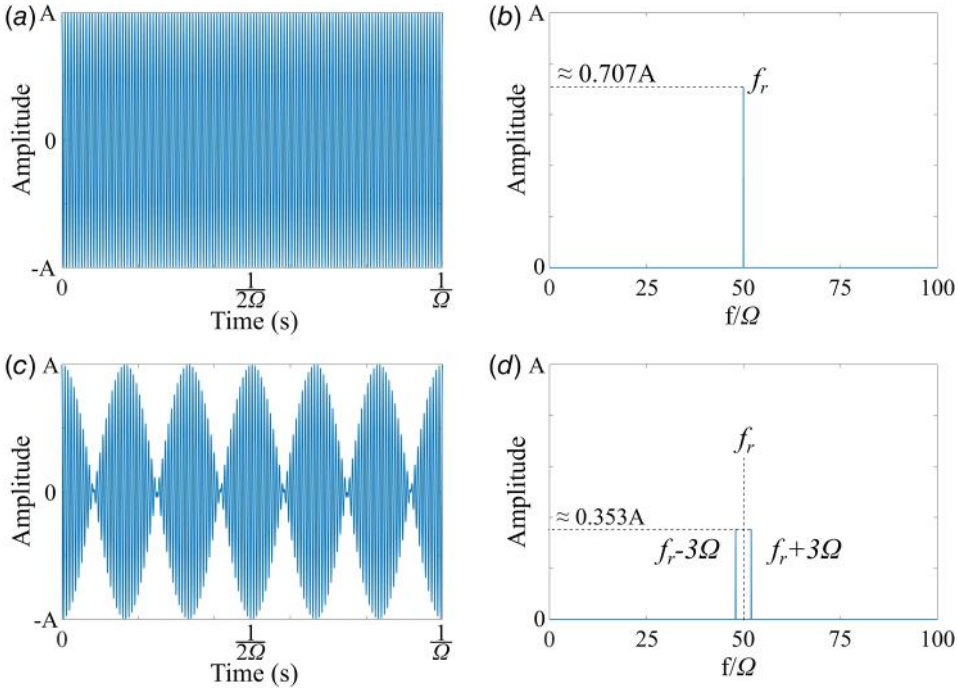

Fig. 3 Frames of reference for $n = 3$ at a resonance frequency $f_r = 100$ Hz: (*a*) rotating frame time signal, (*b*) rotating frame frequency spectrum, (c) stationary frame time signal, and (*d*) stationary frame frequency spectrum

Subsequently, $v(t)$ has been processed through a Butterworth digital low-pass filter, given by

$$u(m) = \frac{1}{a(1)}(b(1)v(m) + b(2)v(m-1) + \ldots + b(mb+1)v(m-mb) - a(2)u(m-1) - \ldots - a(ma+1)u(m-ma)) \tag{12}$$

where u values are the demodulation values in the Y-axis after filtering Eq. (11), a and b are coefficients dependent on the filter requirements, m is the order of the filter, and v values are the data point of the demodulation function in Eq. (11). The values of a and b can be determined using a Butterworth filter designer using the MATLAB R2024B function *butter*. This function is dependent on the order of the filter m and the frequency parameter w_n, defined as

$$w_n = \frac{2f_r}{f_s} \tag{13}$$

where f_s is the acquisition frequency. Later, the demodulation of $w_s(t)$ can be obtained. In Fig. 4, both $w_s(t)$, from Eq. (8), and its demodulation $u(t)$ are graphically shown in blue and orange, respectively. To demodulate $w_s(t)$ from the vibration frequency, the MATLAB R2024B function *amdemod* is implemented.

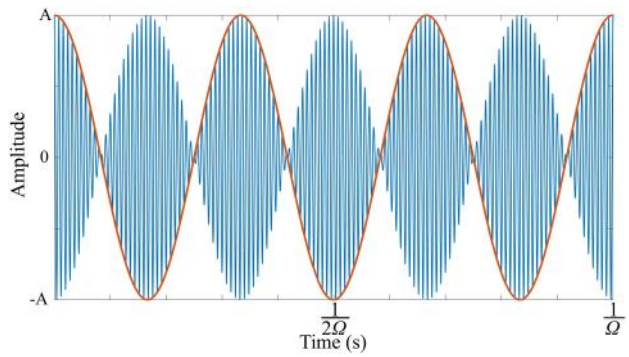

Fig. 4 Amplitude modulated signal for $n = 3$ and its demodulation

2.4 Vibration Frequency Calculation. As aforementioned, the demodulation process is dependent on the vibration frequency f_r. However, this parameter might not always be known and, depending on the modulation of the signal, could be challenging to estimate from the stationary frame. For this reason, the extraction of the vibration frequency from the AM signal is also investigated.

Typically, the instantaneous frequency $f(t)$ of a modulated signal $w(t)$ can be calculated as [42]

$$f(t) = \frac{d}{dt}\left(\tan^{-1}\left(\frac{jH[w_s(t)]}{w_s(t)}\right)\right) \tag{14}$$

where j is the imaginary unit, and H is the Hilbert function, given by the convolution of the function $w_s(t)$ with the signal $1/\pi t$ so

$$H[w_s(t)] = \frac{1}{\pi}\int_{-\infty}^{\infty}\frac{w_s(t-\tau)}{\tau}d\tau \tag{15}$$

where τ is the integration variable. However, this calculation is limited to simple vibration signals and does not have a good performance with amplitude-modulated signals with complicated modulations. In this line, using the Hilbert transform $H[w_s(t)]$, the envelope of the $w_s(t)$ can be calculated as

$$e(t) = \sqrt{w_s(t)^2 + jH[w_s(t)]^2} \tag{16}$$

where the envelope $e(t)$ represents only the positive peak values of $w_s(t)$. It is important to notice that to calculate the envelope $e(t)$ only the AM signal is needed. This envelope can be calculated using the MATLAB R2023B function *envelope*, as graphically shown in the orange line in Fig. 5.

Considering that the demodulation of the signal takes the positive and negative peaks of the AM signal and the envelope considers only the positive ones, it can be inferred that the absolute value

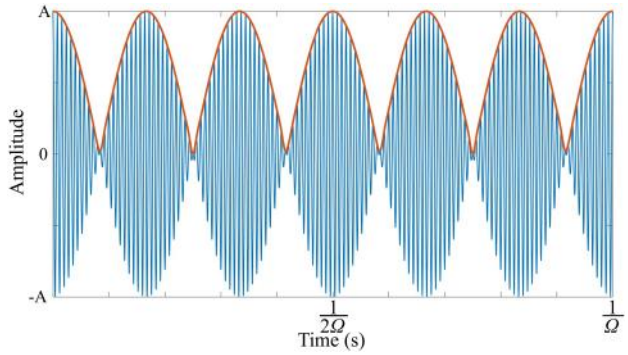

Fig. 5 Amplitude modulated signal for $n = 3$ and its envelope

of the demodulation $u(t)$ may be equivalent to the envelope $e(t)$, such that

$$e(t) = |u(t)| \tag{17}$$

With Eq. (17), an iterative procedure can be performed to calculate the vibration frequency f_r from the modulated signal $w_s(t)$. The calculation routine proposed of this purpose is schematically shown in Fig. 6.

In this routine, the envelope $e(t)$ is calculated by taking the signal $w_s(t)$ as the input. In parallel, $w_s(t)$, the acquisition frequency f_s and an initial value for the vibration frequency $f_{r,0}$ are used to calculate the first demodulation of $u(t)_{i=1}$. Once the vectors corresponding to $e(t)$ and $|u(t)_{i=1}|$ are obtained, the similarity between them is examined through their collinearity using the cosine similarity. For this, the cosine of the angle between $e(t)$ and $|u(t)_{i=1}|$ is calculated using the definition of the dot product [43], such that

$$\cos\left(\alpha_{e/|u|}\right)_i = \frac{e(t) \cdot |u(t)_i|}{||e(t)||\ |||u(t)_i|||} \tag{18}$$

where $\alpha_{e/|u_i|}$ is the angle between $e(t)$ and $|u(t)_i|$. The more similar $e(t)$ and $|u(t)_i|$ are, the smaller is the angle $\alpha_{e/|u_i|}$ between them, and therefore, the closer the value of $\cos\left(\alpha_{e/|u_i|}\right)$ is to 1. With 1 representing a perfect collinearity (from herein referred to as similarity). The calculation process shown in Fig. 6 is repeated for each vibration frequency $f_{r,i}$ in a range from $f_{r,0}$ to $f_{r,f}$, with the frequency increasing by δf_r at each iteration. Then, each of the $f_{r,i}$ and $\cos\left(\alpha_{e/|u|}\right)_i$ values is stored in the vectors $f_{r,v}$ and λ_v, respectively, until $f_{r,f}$ is reached. Once these vectors are obtained, the maximum value of λ_v and its position i in the vector are determined. Finally, the vibration frequency f_r of the modulated signal $w_s(t)$ is given by the element with the position i in the vector $f_{r,v}$.

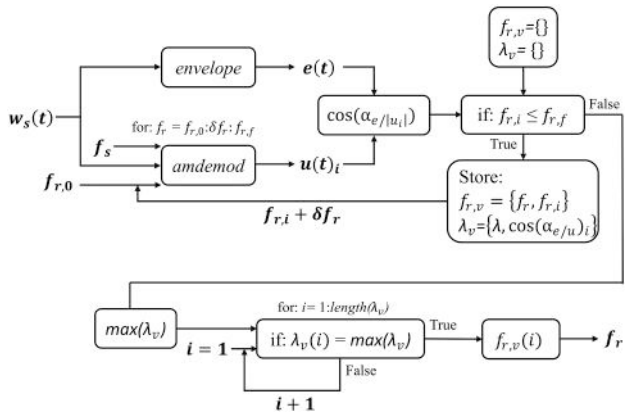

Fig. 6 Algorithm to determine f_r from $w_s(t)$

3 Experimental Procedure

3.1 Experimental Setup. To investigate the determination of mode shapes and natural frequencies from the stationary frame for rotating structures, an experimental test rig has been developed (see Fig. 7(*a*)). In this test rig, the structure to study (see Figs. 7(*b*)–7(*d*)) is attached to a hollow shaft, which is connected to a variable-speed electric motor with a transmission belt. The stainless steel shaft has a length of 350 mm, with an outer diameter of 50 mm and an inner diameter of 20 mm. This shaft is mounted on a base using an axial bearing. This base is attached to a pair of rigid beams that are affixed to a solid wall. The electric motor, on the other side, is directly fixed to the solid wall, so it is connected to the rotating structure only by the transmission belt. In addition, this test rig is equipped with a slip ring, which allows the structure to be excited and its response to be measured from the rotating frame while rotating. Pictures of the used test rig and studied structures are shown in Fig. 7.

In this study, three types of structures are tested: a simple disk (SD), a DBD structure, and a BD (see Figs. 7(*b*)–7(*d*) and Fig. 8). On the one hand, the SD is made out of structural steel. On the other hand, DBD and BD structures are made out of stainless steel. All the structures have an outer diameter of 400 mm. Moreover, the SD and the blades of the BD have a thickness of 8 mm. Conversely, the DBD structure is made out of two disks and seven blades with a thickness of 3 mm and 4 mm, respectively.

3.2 Instrumentation and Equipment. To perform the following experiments, the disk has to be excited with different types of excitations. For this purpose, a light piezoelectric patch (PZT) P-876.A12 DuraAct Patch Transducers (3.5 g) is attached to each structure under study. The desired excitation signal is coded with a computer and loaded onto a National Instruments 9263 signal generator, which produces a voltage output matching the excitation signal. This output is then sent to an OEM835 signal amplifier, activating the piezoelectric patch within a range from −100 V to 250 V, and consequently, exciting the structure. To measure the response of the studied structure from the rotating frame, an accelerometer Dytran 3006A, with a sensitivity of 10 mV/(m/s^2), is attached to the structure. Conversely, to measure the response of the structure from the stationary frame, an LDV Polytec PDV 100 with a sensitivity of 8 mV/(mm/s) is used. Both excitation and response signals are recorded by a Brüel & Kjær Type 3053-B-120 acquisition system, using a sampling frequency of 32,769 samples/s. Finally, to drive the shaft of the test rig, a variable-speed electric motor Mavilor MLV-072 is used. This motor is controlled and stabilized by an Infranor CDI-a motor driver. A scheme of the instrumentation and equipment used in this work is shown in Fig. 9.

3.3 Experiments

3.3.1 Experimental Modal Analysis. In order to determine the natural frequencies and mode shapes of the studied structures in a standstill condition, an experimental modal analysis is carried out. Due to the physical limitations of the test rig, the response of each structure is measured with the LDV only at its periphery, in the points schematically shown in Fig. 10.

Using the PZT, the rotating structures are excited with a chirp frequency-shaped excitation, ranging from 0 Hz to 1600 Hz (see Fig. 11). Each excitation lasts 8 s. After this time, the excitation stops for 4 s, and then the structures are excited again. This procedure is repeated up to five times. In this process, both the excitation (PZT) and response (accelerometer and LDV) signals are recorded.

3.3.2 Numerical Modal Analysis. Since the experimental modal analysis is conducted only on the periphery of the studied structures, a numerical modal analysis (NMA) is also carried out to validate the experimental modal analysis (EMA) performed before. This allows for the analysis of not only the mode shape

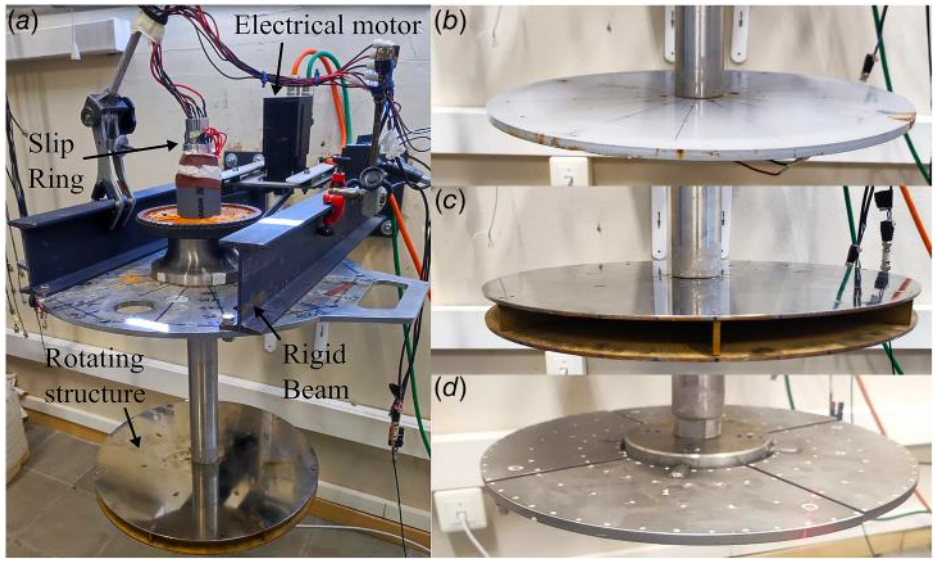

Fig. 7 Test rig: (*a*) test rig used. Rotating structures: (*b*) disk, (*c*) disk-blades-disk structure, and (*d*) bladed disk.

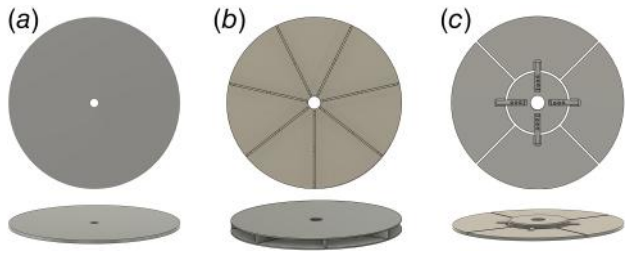

Fig. 8 Tested structures: (*a*) simple disk (SD), (*b*) DBD structure, and (*c*) BD

on the periphery but also across the entire surface of the structures. To do this, the modal module of ANSYS 2020 R2 is used to numerically determine the natural frequencies and mode shapes of the tested structures. The different geometries are modeled using meshes of 250,000 elements and a rigid fixed support condition at the top of the shafts, as indicated in Fig. 12.

3.3.3 Resonance of the Structure in Rotation. After determining the natural frequencies and mode shapes of interest for all the structures, these are put in resonance while rotating at rotating frequencies Ω of 1, 3, and 6 Hz. Measurements of the response during the resonant state are carried out within the periphery of the structures, from both the rotating and the stationary frames (see Fig. 10). An example of the excitation signal and responses of SD rotating at 3 Hz, detected from both the stationary and rotating frames, is shown in Fig. 13.

4 Results

4.1 Natural Frequencies and Mode Shapes for Still Structures. To determine the natural frequencies and mode shapes of each structure, the time-domain signals obtained for

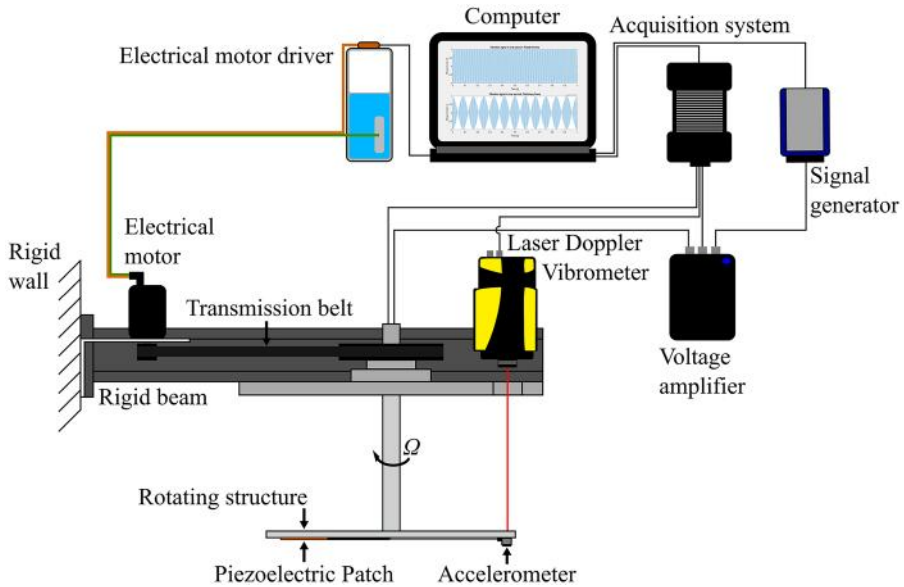

Fig. 9 Schematic connection of the instrumentation and equipment

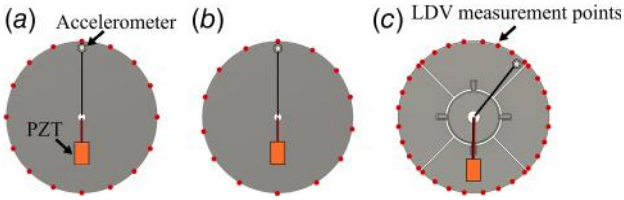

Fig. 10 Location of the measured points during the EMA: (*a*) SD, (*b*) DBD, and (*c*) BD

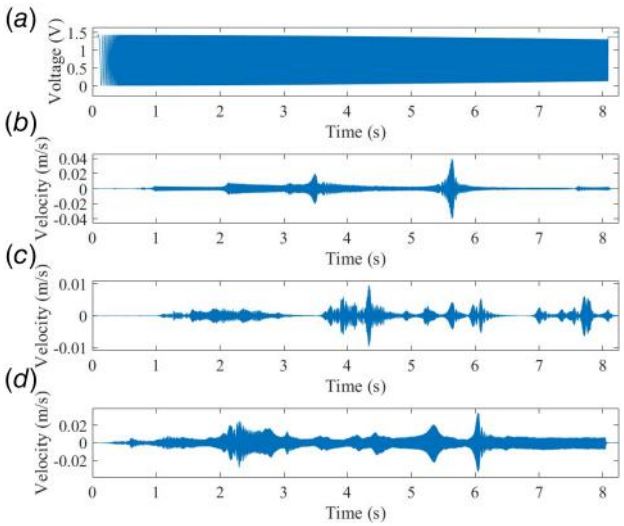

Fig. 11 Chirp test: (*a*) excitation signal, (*b*) response of SD, (*c*) response of DBD, and (*d*) response of BD

the experimental modal analysis were processed using the fast Fourier transform (FFT). As previously explained, the excitations lasted 8 s and were repeated five times for each measured point. For this reason, the time-domain signals from the tests were windowed using a uniform window of 8 s. Later, the FFT was applied to each of the five windows obtained from the original signal with a frequency resolution of 0.125 Hz, and the resulting spectra were averaged. The average spectra obtained from each structure at one single point are shown in Fig. 14.

In Fig. 14(*b*), the averaged frequency spectrum from the disk excitation signal is shown. It can be observed that the PZT excited the disk with a frequency ranging from 0 Hz to 1600 Hz, as previously mentioned. As the excitation signal is the same for all the structures, a similar behavior was exhibited by the excitation frequency spectra from DBD and BD. For this reason and for the sake of avoiding redundancy, these last spectra are not included in Fig. 14.

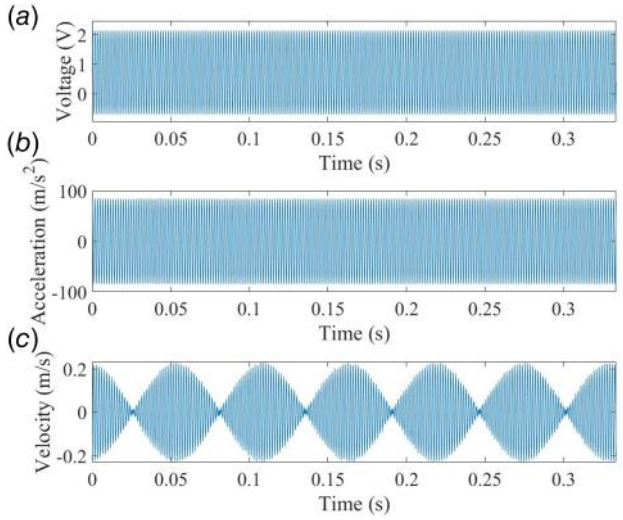

Fig. 13 Resonance of SD at $\Omega = 3$ Hz excited at 295.875 Hz: (*a*) excitation signal, (*b*) response from the accelerometer (rotating frame), and (c) response from the LDV (stationary frame)

Regarding the frequency responses of the studied structures and the mode shapes of interest for this study, the first three diametrical mode shapes were studied for the SD (see Fig. 14(*b*)). In the case of the DBD, as shown in Fig. 14(*c*), only the first three diametrical mode shapes that exhibited an on-phase motion of the upper and lower disks of the structure were studied (according to the description of Presas et al. [38]). In these modes, the in-phase motion of the two disks allows the system to be effectively considered as a single disk. Finally, for the BD, two diametrical mode shapes and one mode shape with both nodal diameters and a circle were chosen for study (according to the classification of Moraga et al. [44]).

By means of NMAs, the EMA on the periphery of the structures was complemented in order to determine the mode shape not only in the periphery of the structure but also in its entire body. In Table 1, a comparison is made between the mode shapes obtained by the EMA conducted on the periphery of the structures and the NMA. In order to simplify the nomenclature for this study, the three studied mode shapes will be called Mode 1, Mode 2, and Mode 3 for SD, DBD, and BD until the end of this work.

It can be observed that for most of the cases, an EMA within the periphery of the structure is enough to determine its mode shape when these are mainly diametrical. It also can be seen that the relative error between the experimental and simulated frequencies is very small in most of the cases, and the mode shapes are very similar. However, for Mode 3 of the DBD and the BD, the relative error escalated to 8.5% and 7.6%, respectively. This could be due to manufacturing and assembling issues of the real structure, which

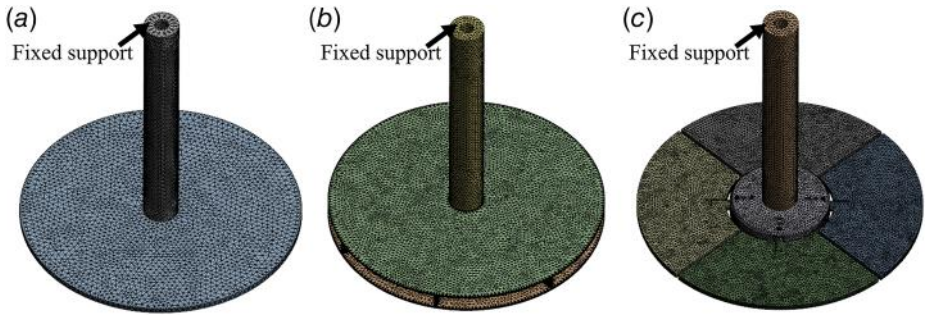

Fig. 12 Mesh for numerical modal analysis: (*a*) SD, (*b*) DBD, and (c) BD

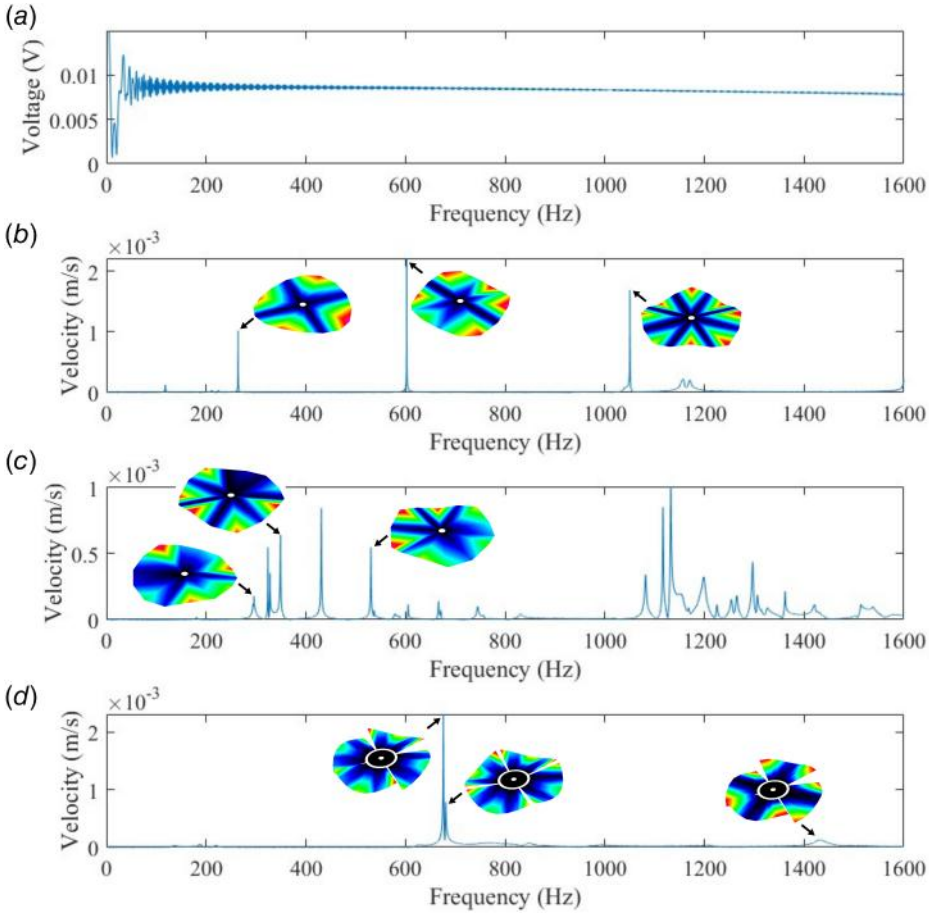

Fig. 14 Spectrums and studied mode shapes: (*a*) PZT, (*b*) SD, (c) DBD, and (*d*) BD

are not considered in the simulation, such as welding, tightness of screws, and friction.

4.2 Natural Frequencies and Mode Shapes for Rotating Structures

4.2.1 Frequency-Domain Analysis. As explained before, the three analyzed structures were put in resonance while rotating, and measurements from both the rotating and stationary frames were carried out using an accelerometer and an LDV, respectively. After recording, the time signal of every case was processed by means of the FFT, using uniform windows of 8 s each. In Fig. 15, the frequency responses of the structures in resonance at the different mode shapes and rotating speeds are summarized. These responses were calculated with a frequency resolution of 0.125 Hz and are shown with respect to a normalized frequency defined as

$$f_{\text{nor}} = \frac{f - f_r}{\Omega} \tag{19}$$

where f represents the X-axis values, and f_r is the resonance frequency.

Due to the normalization of the frequency axis, the response of the structures at the different mode shapes can be analyzed independently of the rotating speed. With this, it can be observed that the response of the sensor from the stationary frame is influenced mainly by the structure and its mode shape. In the case of the SD (see Figs. 15(*a*)–15(*c*)), for instance, it can be seen that the peaks obtained from the stationary frame are separated by $\pm n$ from the resonance frequency measured from the rotating frame (considering n as the number of nodal diameters in the mode shape), as explained by Presas et al. [26].

It can also be observed that the more complex the structure and its mode shapes, the more components are detected in the response from the stationary frame. On the one hand, for the case of DBD (see Figs. 15(*d*)–15(*f*)), four main components, dependent on both the number of nodal diameters and the number of blades in the structure, it can be seen (in line with the observations done by Presas et al. [38]). On the other hand, for the case of BD (see Figs. 15(*g*)–15(*h*)), it can be noticed that its response from the stationary frame not only depends on the mode shape and the number of blades but also on the phase shift between the blades. Mode 2 of BD and Mode 3 of SD exhibited a similar nodal line distribution, deformation, and response from the stationary frame. In this case, BD behaved like a simple disk, and only two main components were detected. Conversely, from Mode 1 of BD (see Fig. 15(*g*)), for the same number of nodal diameters as Mode 2 but with a counter-phase motion of the blades with respect to each other, multiple components were detected from the stationary frame.

It is worthy to mention that although small equidistant peaks are observed in most of the charts in Fig. 15, these are components of the rotation speed and could be caused by the unbalance of the rotor of the test rig.

As shown in Fig. 15, conducting measurements on a rotating structure from the stationary frame leads to the detection of numerous components in its frequency response. The complexity of the rotating structure and its mode shapes can make the analysis of its frequency response from the stationary frame challenging for the identification of the natural frequencies of the structure. This complexity may be increased if components from other sources, such as those from the operation of a nearby machine, are detected.

4.2.2 Time-Domain Analysis. Due to the challenges exposed in the analysis of the frequency response and the determination

Table 1 Studied mode shapes and natural frequencies

	Mode 1	Mode 2	Mode 3
SD	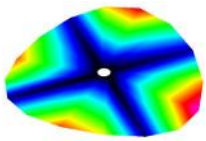	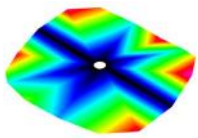	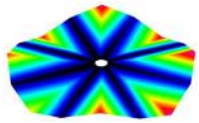
EMA	264.125 Hz	602.625 Hz	1050.875 Hz
SD	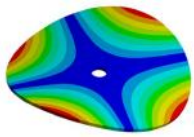	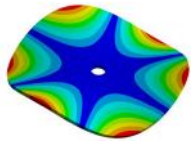	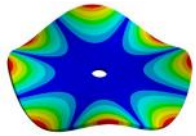
NMA	271.470 Hz	601.200 Hz	1050.900 Hz
Relative error	2.705%	0.237%	0.002%
DBD	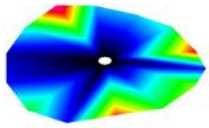	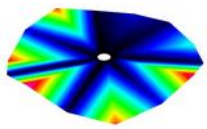	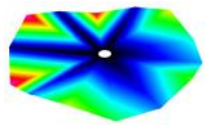
EMA	295.875 Hz	349.125 Hz	605.375 Hz
DBD	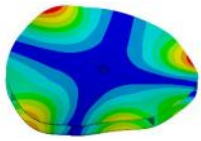	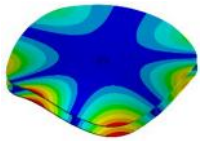	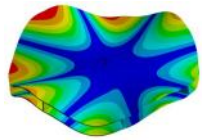
NMA	294.660 Hz	350.650 Hz	557.710 Hz
Relative error	0.412%	0.435%	8.546%
BD	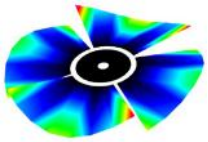	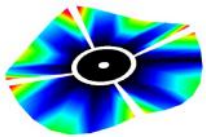	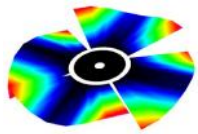
EMA	676.000 Hz	680.625 Hz	1427.875 Hz
BD	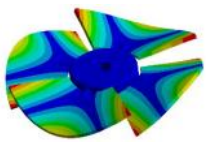	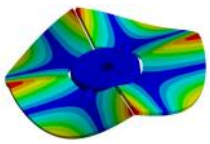	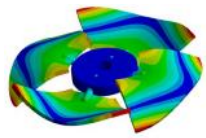
NMA	677.510 Hz	674.480 Hz	1327.100 Hz
Relative error	0.223%	0.911%	7.593%

of the mode shapes of a rotating structure from the stationary frame, another method was explored. For this, the time-domain response signals from the rotating structures in resonance were acquired from the stationary frame and later analyzed. As shown in Figs. 16(*a*)–16(*c*), the AM modulation of the LDV signals was observed. However, noise and undesired components for this analysis were also detected. Therefore, the AM signals were filtered with a band-pass filter, considering a band of $f_r \pm 50$ Hz.

After filtering, a clearer amplitude modulation of the LDV signals due to the motion of the periphery of the rotating structure was obtained (see Figs. 16(*d*)–16(*f*) in blue). By applying the demodulation process described in Sec. 2.3 to the filtered AM signal, the mode shape of the rotating structure periphery was determined (see Figs. 16(*d*)–16(*f*) in orange).

In the aforementioned procedure, each demodulation was obtained for a single revolution. Next, to calculate an average deformation of the periphery and then to obtain the mode shape of each structure, the demodulations of 20 revolutions were linearly averaged. This procedure was systematically repeated for all the tested structures, mode shapes, and rotating speeds. The obtained averaged periphery deformations for all the structures are summarized in Fig. 17. In this figure, the deformations are shown with respect to a normalized amplitude A_{nor} and a normalized time τ. On the one hand, the normalized amplitude A_n is given by

$$A_{\text{nor}} = \frac{A}{A_{\text{max}}} \tag{20}$$

where A represents the Y-axis values for each demodulation, and A_{max} represents the maximum absolute value for each demodulation. On the other hand, the normalized time τ is defined as

$$\tau = t_{\text{rev}} * \Omega \tag{21}$$

where t_{rev} is the X-axis values for a single revolution, and Ω is the rotating speed.

In Fig. 17, all measured mode shapes are summarized and compared for each structure at different rotating speeds. The black dots represent the deformation of the structure at different angular positions obtained from the EMA. The results shown in this figure indicate that the mode shape at the structural periphery can be consistently obtained across the tested rotational speeds, with good agreement between low and high speeds. It can also be seen that complex mode shapes, such as those from the DBD (see Figs. 17(*d*) and 17(*e*)), may be more challenging to obtain with the present procedure at high rotating speeds. Therefore, some differences among the periphery deformation curves

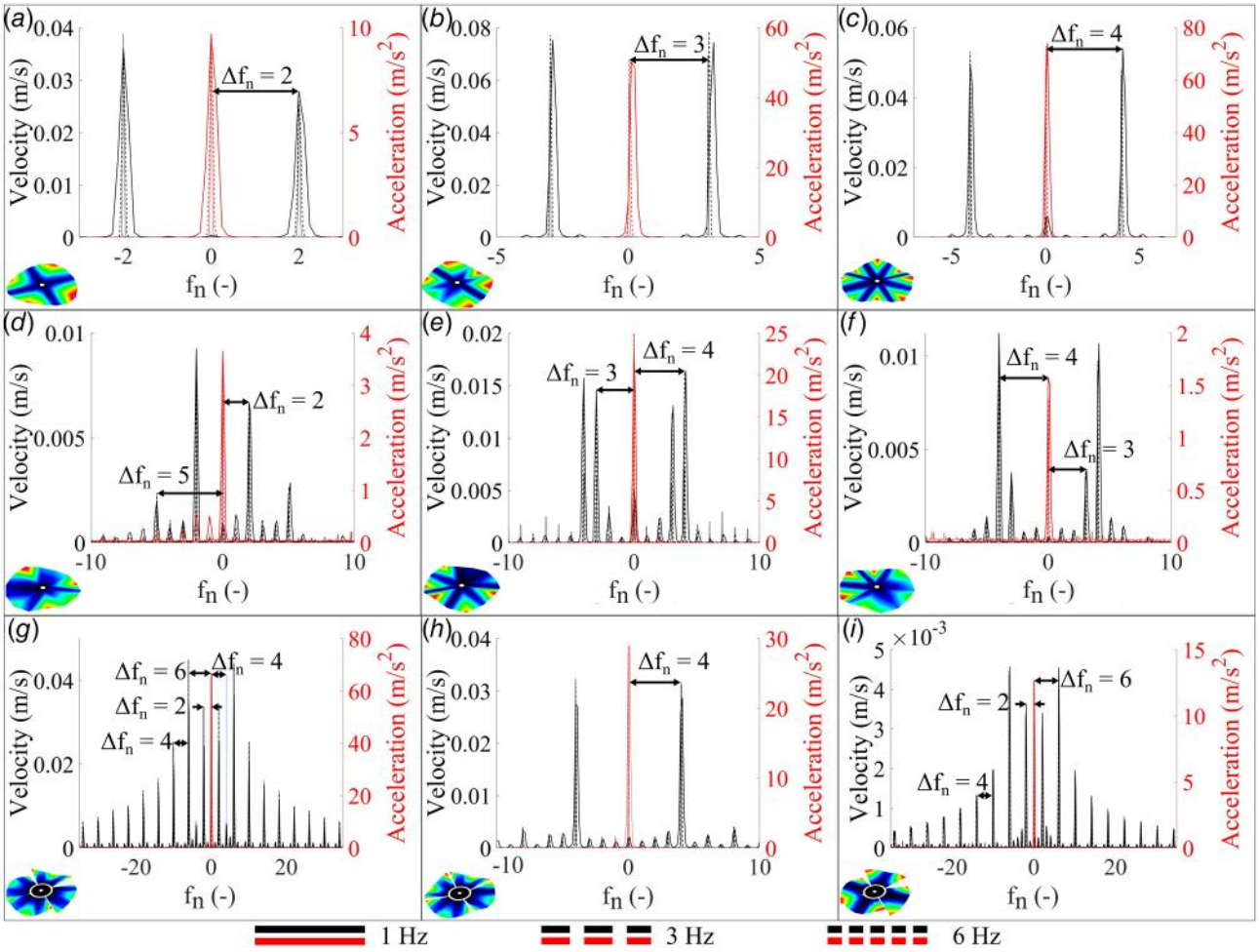

Fig. 15 Response of the structures in the frequency domain from the rotating frame (black) and the stationary frame (red): (*a*) SD—Mode 1, (*b*) SD—Mode 2, (*c*) SD—Mode 3, (*d*) DBD—Mode 1, (*e*) DBD—Mode 2, (*f*) DBD—Mode 3, (*g*) BD—Mode 1, (*h*) BD—Mode 2, and (*i*) BD—Mode 3

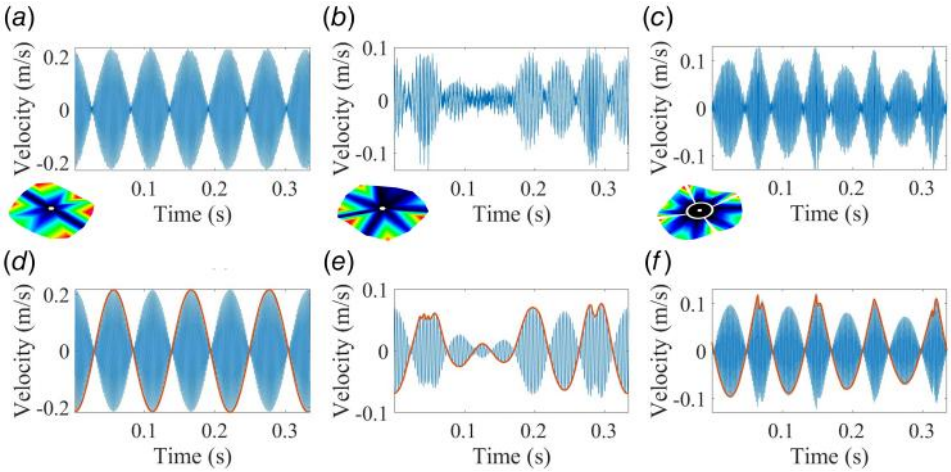

Fig. 16 LDV signal from one revolution for a rotating speed of 3 Hz at Mode 2 of (*a*) SD, (*b*) DBD, and (*c*) BD. Filtered LDV signal and demodulation from one revolution for a rotating speed of 3 Hz at Mode 2 of (*a*) SD, (*b*) DBD, and (*c*) BD.

obtained at the different rotating frequencies can be detected for a single mode shape.

The relative amplitudes measured at each point during the EMA were compared with those obtained at each angular position for different rotating speeds. This comparison is performed using the cosine similarity, as defined in Eq. (18). For the present case, the cosine similarity is defined as the cosine of the angle between two vectors: the vector of normalized relative amplitudes

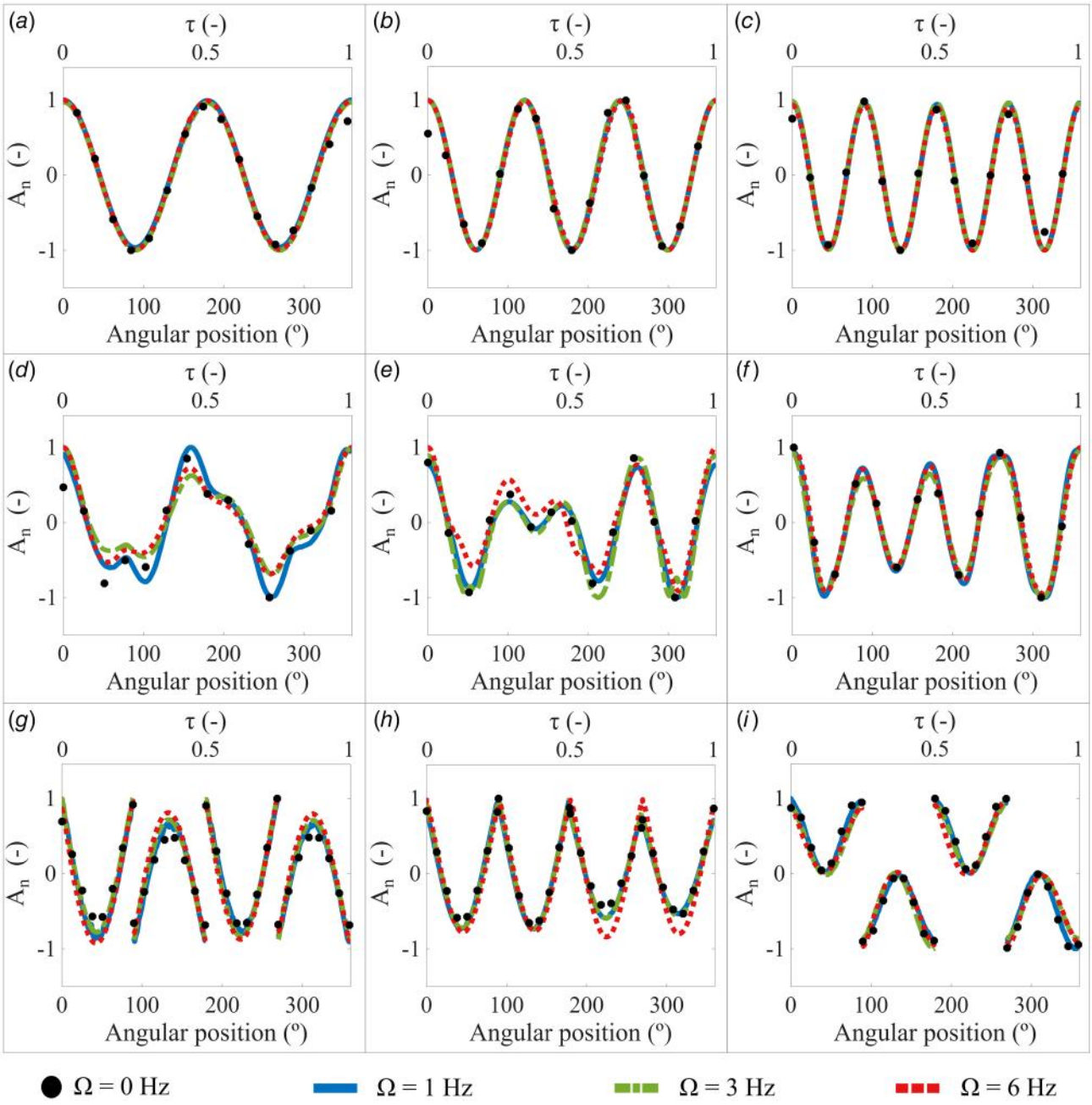

Fig. 17 Deformation of the rotating structure periphery at different rotating speeds for SD: (*a*) Mode 1, (*b*) Mode 2, and (c) Mode 3. For DBD: (*d*) Mode 1, (e) Mode 2, and (*f*) Mode 3. For BD: (*g*) Mode 1, (*h*) Mode 2, and (*i*) Mode 3.

Anor0(θ), measured under standstill conditions at different angular positions (EMA), and the vector, Anor$\Omega(\theta)$ measured at the same angular positions when the structure rotates at angular speed Ω with the mode shape i. Then the cosine similarity for each structure is given by

$$\cos\left(\alpha_{\text{Anor0}i/\text{Anor}\Omega i}\right)_{\text{structure}} = \frac{\text{Anor0}(\theta)_i \cdot \text{Anor}\Omega(\theta)_i}{||Anor0(\theta)_i||\ ||\text{Anor}\Omega(\theta)_i||} \tag{22}$$

Table 2 summarizes the cosine similarity values described above for all combinations of structures, mode shapes, and rotating speeds. It can be observed that the similarity does not fall below 0.88, which indicates a general good level of agreement between the mode shapes extracted under rotating conditions and those obtained from the EMA.

By plotting the peripheral deformation curves on a polar plot, the mode shapes of the structures obtained in rotation can be compared with those obtained in a standstill condition through modal analysis. In Fig. 18, the results obtained for Mode 2 of each structure through modal analyses are contrasted with those obtained using the current method while every structure is rotating in resonance at 3 Hz. It can be seen a good resemblance among the mode shapes detected at the standstill condition and those obtained from the stationary frame while the structure was rotating.

In Mode 2 of DBD (see Fig. 18(*h*)), there are observable differences in the zones of maximum amplitude when compared to Fig. 18(*b*), which is considered its reference. In these zones, two of the maximum amplitude areas appear to be split. This issue could occur during the signal filtering process. The time-domain signal of the DBD vibrating at its Mode 2 is shown in Fig. 16(*b*) where two zones with a characteristic noise can be observed at

Table 2 Cosine similarity between the mode shapes obtained at different rotating speeds and those obtained in the standstill condition (EMA)

Structure	Ω (Hz)	$\cos(\alpha_{Anor01/Anor\Omega1})$	$\cos(\alpha_{Anor02/Anor\Omega2})$	$\cos(\alpha_{Anor03/Anor\Omega3})$
SD	1	0.9929	0.9834	0.9927
	3	0.9949	0.9845	0.9925
	6	0.9944	0.9807	0.9932
DBD	1	0.9519	0.9801	0.9890
	3	0.8874	0.9592	0.9907
	6	0.9153	0.9398	0.9959
BD	1	0.9867	0.9725	0.9963
	3	0.9874	0.9844	0.9900
	6	0.9800	0.9800	0.9850

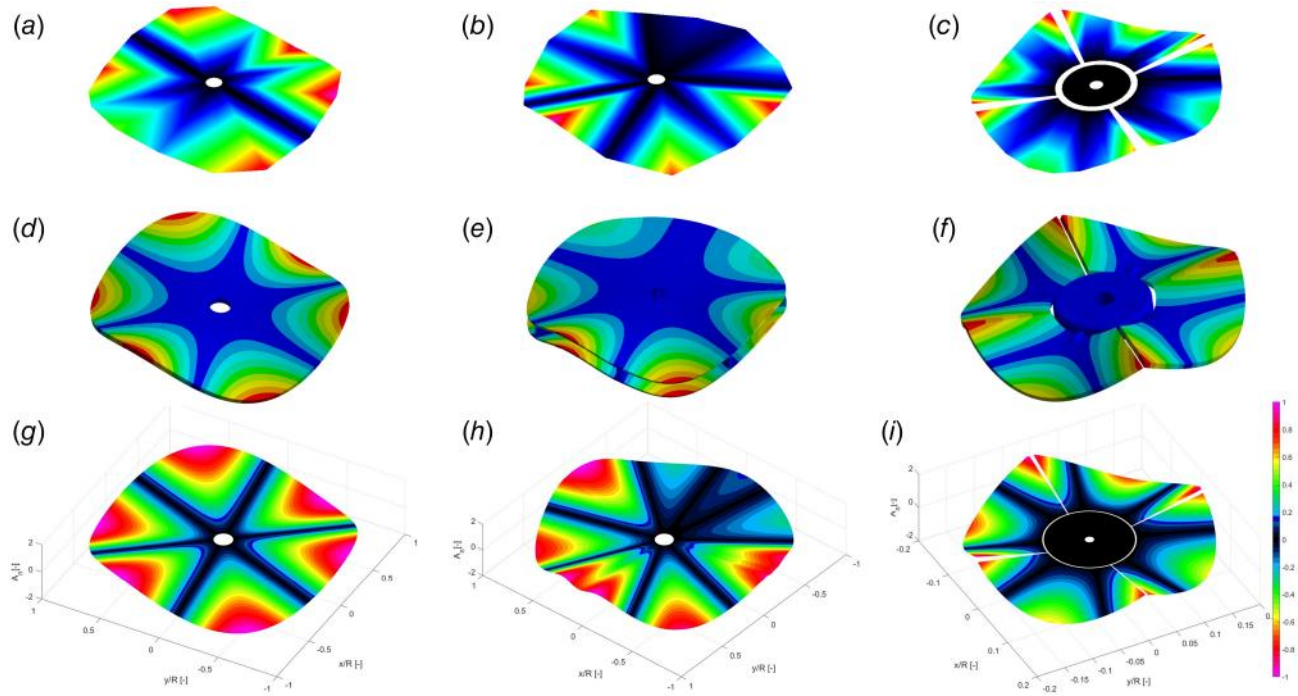

Fig. 18 Mode 2 from EMA for (*a*) SD, (*b*) DBD, and (*c*) BD. Mode 2 from NMA for (*d*) SD, (*f*) DBD, and (*g*) BD. Mode 2 obtained from the proposed methodology at a rotation frequency of 3 Hz: (*h*) SD, (*i*) DBD, and (*j*) BD.

approximately 0.05 s and nearly 0.3 s. However, after the signal was filtered, these two zones of maximum amplitude were noticeably affected, as shown in Fig. 16(*e*). This issue was not observed for Mode 2 of the DBD structure when it was rotating at either 1 Hz or 6 Hz, as shown in Fig. 17(*e*).

Finally, to study the accuracy of determining the natural frequencies by means of the analysis of their time-domain response, the algorithm schematically shown in Fig. 6 was implemented. With this, the natural frequencies for all the mode shapes were calculated for different rotating speeds. These frequencies were then

Table 3 Natural frequencies calculated from the time-domain signal for the studied structures

Structure	Rotating frequency (Hz)	Mode 1 frequency (Hz)	Mode 2 frequency (Hz)	Mode 3 frequency (Hz)	Mode 1 RE (%)[a]	Mode 2 RE (%)[a]	Mode 3 RE (%)[a]
SD	1	264.152	602.809	1050.981	1.022×10^{-2}	3.053×10^{-2}	1.008×10^{-2}
	3	264.141	602.809	1080.987	6.058×10^{-3}	3.053×10^{-2}	1.065×10^{-2}
	6	264.149	602.809	1050.979	9.087×10^{-3}	3.053×10^{-2}	9.897×10^{-3}
DBD	1	295.905	349.161	605.433	1.013×10^{-2}	1.031×10^{-2}	1.008×10^{-2}
	3	295.900	349.167	605.434	8.450×10^{-2}	1.203×10^{-2}	9.735×10^{-3}
	6	295.914	349.154	605.433	1.318×10^{-2}	8.306×10^{-3}	9.735×10^{-3}
BD	1	676.076	680.718	1428.019	1.124×10^{-2}	1.366×10^{-2}	1.008×10^{-2}
	3	676.064	680.695	1428.014	9.467×10^{-3}	1.028×10^{-2}	9.735×10^{-3}
	6	676.072	680.674	1428.014	1.065×10^{-2}	7.199×10^{-3}	9.735×10^{-3}

[a]RE (%): relative error with respect to the frequencies measured in the EMA.

compared with those obtained from the EMA. The natural frequencies obtained, along with the relative errors with respect to those frequencies obtained from the EMA, are summarized for the different structures in Table 3. As can be observed, the natural frequencies for each case were calculated with a significantly low error when compared to the natural frequencies obtained from the EMA, showing the feasibility of the determination of the natural frequencies for a rotating structure in resonance with good accuracy with the presented methodology.

With the present procedure, it has been demonstrated that the determination of mode shapes and natural frequencies of a rotating structure in resonance can be accurately performed from the stationary frame for the mode shapes that behave as standing waves.

4.3 Relevant Parameters for the Mode Shape Extraction. In order to determine the limitations of the presented methodology, the influence of parameters, such as the rotating frequency, the sampling frequency, and the mode shape, on the demodulation process, was analytically studied. For this, the response of the periphery of a simple disk vibrating in resonance at a frequency f_r, at a diametrical mode shape n and rotating at a frequency Ω was modeled over the time domain using Eq. (7), considering the stationary frame perspective. After the response was modeled, the aforementioned demodulation process was carried out in order to obtain the mode shape. First, to study the influence of the rotating frequency, Eq. (7) was evaluated for rotating speeds from 1% to 100% of f_r. Moreover, to study the influence of the sampling frequency, the modeled signal was generated at a sampling frequency f_s from 2.01 to 20 times f_r. Then, the demodulations of all the generated signals were compared with a reference demodulation by means of the examination of their collinearity, using Eq. (18). The reference demodulation was obtained from a theoretical response signal at a low rotating speed modeled using Eq. (7), in order to obtain a high number of vibration cycles per revolution, and generated with a high number of points per vibration cycle. Therefore, the reference signal rotating speed was chosen to be at a 1% f_r and generated with a sampling frequency of 200 times f_r. Lastly, in order to analyze the influence of the mode shape on the demodulation process, this analysis was conducted for the same first three diametrical mode shapes studied before for the SD.

The results from the comparison between each demodulation and the reference, for every rotating frequency, sampling frequency, and mode shape, are summarized in contour plots in Fig. 19. As the aim of this analysis is to show the limitations of the demodulation process, these plots show the similarity between the demodulation of each signal and the reference for values ranging from 0.8 to 1, where the performance of the method is higher, 1 represents the maximum collinearity and, therefore, the maximum similarity to the reference. These values are plotted with respect to the ratio between the rotating frequency and the resonance frequency on the *Y*-axis, and the ratio between the sampling frequency and the resonance frequency on the *X*-axis.

From Fig. 19, it can be observed that as the ratio f_s/f_r increases, the similarity between the tested and the reference demodulations also increases. However, within the zone of rotating frequencies under 10% f_r for every mode shape, it is possible to see that when the ratio f_s/f_r reaches values above 3, the similarity remains at its maximum. Therefore, for rotating speeds lower than 10% f_r, high sampling frequencies are not needed to reach an accurate demodulation of the AM signal. On the other hand, regarding the influence of the rotating speed on the demodulation process, it can be seen that the similarity between the tested demodulation and the reference gradually decreases at rotating frequencies higher than 10% f_r. From this point, it can be observed that at higher rotating frequencies, a higher similarity can be reached by increasing the sampling frequency. On the other hand, the rate of decrease of the similitude due to the increasing rotating frequency is directly influenced by the tested mode shape. When the order of the mode shapes increases, and therefore, the complexity of the amplitude modulation of the signal increases, the rotating speed range at which the similarity remains high decreases. From Fig. 19, it can be seen that for Mode 1, the similarity between the tested demodulation and the reference remained nearly at the maximum for rotating speeds up to a limit of 50% f_r, approximately, for a sampling frequency of 20 times f_r. After this limit, the similarity drastically decreased. For Modes 2 and 3, the same behavior was observed at the same sampling frequency. However, the similarity between the tested demodulation and the reference, remained nearly at the maximum for rotating speeds up to 33% f_r and 25% f_r, respectively, also decreasing drastically after these limits.

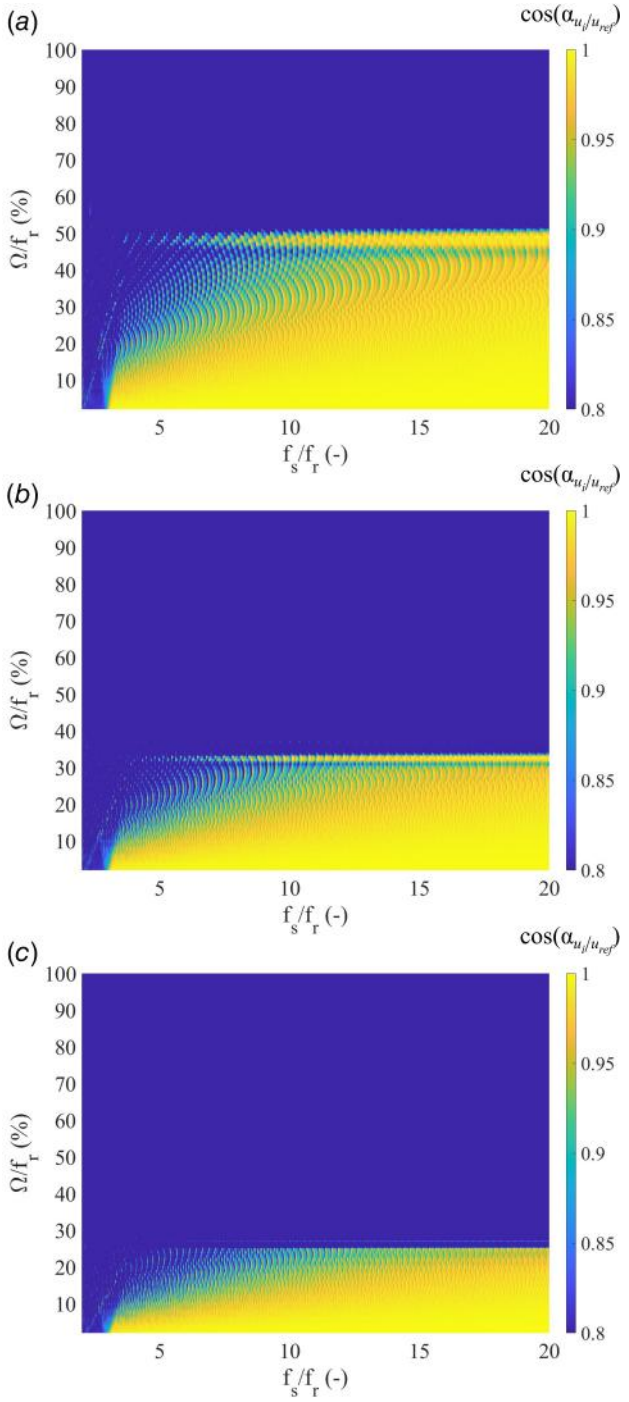

Fig. 19 Limitations for the methodology with respect to the rotating and sampling frequencies for a theoretical SD vibrating at (*a*) Mode 1, (*b*) Mode 2, and (*c*) Mode 3

5 Final Remarks and Domain of Application

Despite the limitations discussed in the previous section, the proposed methodology provides a reliable framework for measuring the natural frequency and the excited standing-wave mode shape of a structure in resonance from a stationary frame. As previously mentioned, the application of this methodology in real turbomachinery strongly depends on the ratios f_s/f_r and Ω/f_r. Therefore, the operating conditions of the machine must be considered.

Regarding the measurement of standing mode shapes in rotating disk-like structures, a potential application of this methodology is the analysis of centrifugal compressor impellers. Although these structures operate at speeds ranging from 10,000 rpm to 35,000 rpm, the literature reports natural frequencies between 750 Hz and 5330 Hz [6,45–47]. Based on this information, rough approximations of the ratio Ω/f_r, yield values below 30%. According to Fig. 19(*a*), these values remain within the limit for a lower-order mode shape. Similarly, for axial flow compressor impellers, natural frequencies between 1167 Hz and 7106 Hz have been reported at a rotational speed of 286.47 rpm [48]. In this case, the ratio Ω/f_r ranges from 4% to 24.5%, remaining below the threshold shown in Fig. 19(*a*) for a low-order mode shape. Thus, measuring the mode shapes and frequencies of disk-like structures, such as axial and centrifugal compressor impellers, could be feasible under the previously mentioned operational and structural parameters.

Another potential application of this methodology is the measurement of mode shapes and natural frequencies in bladed structures, such as axial flow fans. Fans with rotational speeds ranging from 1200 rpm to 2651 rpm have been studied in Refs. [49–51], reporting natural frequencies of interest between 101.5 Hz and 2190 Hz. For these cases, the ratios Ω/f_r can be roughly estimated to range from 2% to 24%. Although these values are still below the threshold shown in Fig. 19(*a*) for a disk, a proper analysis of the Ω/f_r ratio should be conducted for the specific bladed structure under study, considering the mode shapes of interest, the gap between the blades and the signal processing techniques applied.

Finally, the findings of Abbas et al. [32] and Uslu et al. [52] suggest that the natural frequencies of a submerged and rotating propeller are not affected by rotation. Based on this, a potential application of the proposed methodology is the measurement of mode shapes and resonant frequencies in submerged bladed structures, such as marine propellers, which can exhibit Ω/f_r ratios between 8% and 16% [52]. Similarly, Valero et al. [53] suggested a comparable effect in a Kaplan turbine under operation, indicating that standing-wave mode shapes could be excited during transient conditions. Reported values for Kaplan turbine runners in the literature suggest that the Ω/f_r can be roughly estimated to range from 1% to 9% [53–55].

6 Conclusions

In this work, the determination of mode shapes and resonant frequencies of rotating structures from the stationary frame was experimentally investigated for three different types of structures: a simple disk, a disk-blades-disk structure, and a bladed disk. These structures were mounted in a dedicated test rig to study their modal behavior while rotating at different speeds. Measurements were performed from both the stationary and rotating frames using an LDV and an accelerometer, respectively.

To determine the mode shapes and natural frequencies of the tested structures in a stationary condition, experimental and numerical modal analyses were conducted. Once the mode shapes and natural frequencies of interest were identified, the tested structures were put into rotation and brought to a resonant state by means of a piezoelectric actuator. Under these conditions, the determination of the mode shapes and resonant frequency was investigated by analyzing the demodulation of the time-domain response signal obtained from the stationary frame with the LDV.

The analysis of the different structural responses in rotation was performed in both the frequency and time domains. In the frequency domain, determining the mode shapes and vibration frequency in resonance proved challenging due to the number and distribution of the components of the structural response spectra, which depended on the geometry and complexity of the excited mode shape. Conversely, in the time domain, using the methodology proposed in this work, the vibration frequency was calculated with very low errors when compared to the excitation frequency. Moreover, by demodulating the structural responses, the mode shapes of the periphery of each structure were determined accurately and closely resembled those obtained through experimental modal analysis.

To determine the limitations of the proposed methodology, the influence of the rotating frequency, sampling frequency, and complexity of the mode shape was analytically studied. It was found that the structural response demodulation accuracy is highly dependent on the rotating frequency. When the ratio Ω/f_r increases, the accuracy of the response signal demodulation decreases. Although this decrease was mitigated by increasing the sampling frequency, the ratio Ω/f_r could only be increased to a certain limit to maintain good accuracy in demodulation. This limit was determined by the mode shape, showing that more complex mode shapes reduce the maximum Ω/f_r value that assures an accurate demodulation. Finally, the sampling frequency f_s showed to be significant for Ω/f_r values higher than 10%. However, for values less than 10%, the quality of the demodulations was not significantly influenced by the sampling frequency as long as it was more than three times the vibration frequency.

Acknowledgment

G.M. received fonding from the National Agency for Research and Development (ANID)/Scholarship Program/DOCTORADO BECAS CHILE/2020–72210054 during the experimental phase and from the project "Diseño y control de centrales hidroeléctricas flexibles por hibridación con baterías de 2ª vida" (FLEXHYBAT, Proyecto J03103—PID2022-139479OB-C21) during the conceptualization of the article. A.P. and D.V. want to acknowledge the Serra Hunter Program of Generalitat de Catalunya.

Conflict of Interest

There are no conflicts of interest.

Data Availability Statement

The datasets generated and supporting the findings of this article are obtainable from the corresponding author upon reasonable request.

Author Contribution Statement

Greco Moraga: conceptualization, data curation, formal analysis, investigation, software, validation, visualization, and writing—original draft; David Valentín: conceptualization, methodology, and software. Xiang Xia: conceptualization and methodology; Mónica Egusquiza: writing—review and editing and methodology; Victor Fernández: conceptualization and writing—review and editing. Alexandre Presas: conceptualization, formal analysis, investigation, methodology, supervision, and writing—review and editing.

Nomenclature

a = coefficient dependent on the filter requirements
b = coefficient dependent on the filter requirements
e = envelope function of a signal (m)

f = frequency vector (Hz)
h = thickness (m)
i = position in vector (iteration variable)
j = imaginary number
m = order of the filter
n = number of nodal diameters
r = radial coordinate (m)
t = time (s)
u = demodulation vector (m)
v = demodulation function definition (m)
A = vibration amplitude (m/s)
$f_{1\text{-}s}$ = lower natural frequency from the stationary frame (Hz)
$f_{2\text{-}s}$ = higher natural frequency from the stationary frame (Hz)
f_{nor} = normalized frequency
f_r = resonance frequency (Hz)
f_s = acquisition frequency (Hz)
I_n = first-order Bessel function
J_n = modified first-order Bessel function
k_{ns} = frequency parameter
t_{rev} = time vector for a single revolution (s)
w_n = frequency parameter for filtering
w_r = displacement from the rotating frame (m)
w_s = displacement from the stationary frame (m)
A_{max} = maximum amplitude (m/s)
A_n = constant determined by the boundary conditions imposed on the structure
A_{nor} = normalized amplitude
A_{nor0} = normalized relative amplitude measured under standstill conditions at different angular positions
$A_{\mathrm{nor}\Omega}$ = normalized relative amplitude measured at the same angular positions when the structure rotates at angular speed Ω
C_n = constant determined by the boundary conditions imposed on the structure

Greek Symbols

$\alpha_{e/|u|}$ = angle between the envelope and the demodulation (rad)
$\alpha_{Anor0i/Anor\Omega i}$ = angle between the normalized relative amplitudes measured in standstill and rotating conditions (rad)
θ = angular coordinate from the rotating frame (rad)
λ_v = vector to save $\cos(\alpha_{e/|u|})_i$
τ = normalized time
ρ_D = disk density (kg/m^3)
φ = angular coordinate from the stationary frame (rad)
ψ = radial deformation function (m)
ω = natural frequency (Hz)
ω_v = natural frequency in vacuum (Hz)
Ω = rotating frequency (Hz)

References

[1] Murthy, S., and Mullican, A., 1993, Transient Performance of Fan Engine With Water Ingestion ,NASA Contractor Report 190778.
[2] Kim, M., Lim, J., and Chung, J., 2016, "Transient Vibration Identification and Reduction of a Centrifugal Fan for a Wall-Installed Air-Conditioner," Trans. Korean Soc. Noise Vib. Eng., **26**(4), pp. 383–390.
[3] Li, Y., Henry, D., Bansal, K., and Rudra, K., 2018, "CFD Modeling and Performance Evaluation of a Centrifugal Fan Using a Cut-Cell Method With Automatic Mesh Generation and Adaptive Mesh Refinement," 24th International Compressor Engineering Conference, West Lafayette, IN, July 9–12.
[4] Xu, C., Zhou, H., and Mao, Y., 2020, "Analysis of Vibration and Noise Induced by Unsteady Flow Inside a Centrifugal Compressor," Aerosp. Sci. Technol., **107**.
[5] Xue, X., and Wang, T., 2019, "Stall Recognition for Centrifugal Compressors During Speed Transients," Appl. Therm. Eng., **153**, pp. 104–112.
[6] Magara, Y., Yamaguchi, K., Miura, H., Takahashi, N., and Narita, M., 2012, "Natural Frequency Shift in a Centrifugal Compressor Impeller for High-Density Gas Applications," ASME J. Turbomach., **135**(1), p. 011014.
[7] Dring, R. P., Joslyn, H. D., Hardin, L. W., and Wagner, J. H., 1982, "Turbine Rotor-Stator Interaction," J. Eng. Power, **104**(4), pp. 729–742.
[8] Gaetani, P., 2018, "Stator-Rotor Interaction in Axial Turbine: Flow Physics and Design Perspective," *Aircraft Technology.*, M. C. Kuşhan, ed., InTechOpen, London, UK, pp. 105–128.
[9] Bejgam, R. R., and James, M. P., 2018, "Identification and Avoidance of Impeller Resonance From Impeller Interference Diagram (Safe—Diagram) for an Open Impeller in an Integrally Geared Centrifugal Air Compressor," ASME 2017 Gas Turbine India Conference GTINDIA2017, Bangalore, India, Dec. 7–8.
[10] Kushner, F., Strickland, R. A., and Shurina, J., 2013, "Rotating Component Modal Analysis and Resonance Avoidance—An Update," Forty-Second Turbomachinery Symposium, Houston, TX, Oct. 1–3.
[11] Kushner, F., Richard, S. J., and Strickland, R. A., 2000, "Critical Review of Compressor Impeller Vibration Parameters for Failure Prevention," 29th Turbomachinery Symposium, Houston, TX, Sept. 18–21, pp. 103–112.
[12] Lerche, A. H., Moore, J. J., and Allison, T. C., 2011, "Experimental Study of Blade Vibration in Centrifugal Compressor Blades," Proceedings of the ASME 2011 Turbo Expo: Turbine Technical Conference and Exposition. Volume 6: Structures and Dynamics, Parts A and B, Vancouver, British columbia, Canada, June 6–10.
[13] Hu, B., and Li, B., 2015, "Blade Crack Detection of Centrifugal Fan Using Adaptive Stochastic Resonance," Shock Vib., **2015**(1), pp. 932–954.
[14] Hassen, M. B., Fakhari, S. M., and Mrad, H., 2023, "Assessment of Crack Growth and Fatigue Life of an Axial Fan Blade Based on a Co-Simulation Approach," Adv. Mater. Sci., **23**(3), pp. 61–79.
[15] Abdullah, O. I., and Schlattmann, J., 2012, "Stress Analysis of Axial Flow Fan," Adv. Theor. Appl. Mech., **5**(1), pp. 263–275.
[16] Patil, S. S., and Jadhav, T. A., 2020, "Modal and Fatigue Analysis of Industrial Centrifugal Fan Impeller," J. Sci. Technol. Res., **9**(4), pp. 492–495.
[17] Rama Rao, A., and Dutta, B. K., 2012, "Vibration Analysis for Detecting Failure of Compressor Blade," Eng. Fail. Anal., **25**, pp. 211–218.
[18] Zhang, M, Liu, Y, Wang, W, Wang, P, and Li, J., 2016, "The Fatigue of Impellers and Blades," Eng Fail Anal., **62**, pp. 208–231.
[19] Baqersad, J., Poozesh, P., Niezrecki, C., and Avitabile, P., 2017, "Photogrammetry and Optical Methods in Structural Dynamics—A Review," Mech. Syst. Signal. Process., **86**(Part B), pp. 17–34.
[20] Sriram, P., Craig, J. I., and Hanagud, S., 1992, "Scanning Laser Doppler Techniques for Vibration Testing," Exp. Tech., **16**(6), pp. 21–26.
[21] Stanbridge, A. B., and Ewins, D. J., 1999, "Modal Testing Using a Scanning Laser Doppler Vibrometer," Mech. Syst. Signal. Process., **13**(2), pp. 255–270.
[22] Stanbridge, A. B., Ewins, D. J., and Khan, A. Z., 2000, "Modal Testing Using Impact Excitation and a Scanning LDV," Shock Vib., **7**(2), pp. 91–100.
[23] La, J., Choi, J., and Wang, S., 2003, "Continuous Scanning Laser Doppler Vibrometer for Mode Shape Analysis," Opt. Eng., **42**(3), p. 730.
[24] Stanbridge, A. B., Martarelli, M., and Ewins, D. J., 2004, "Measuring Area Vibration Mode Shapes With a Continuous-Scan LDV," Measurement (Lond), **35**(2), pp. 181–189.
[25] Xu, Y. F., Chen, D. M., and Zhu, W. D., 2020, "Modal Parameter Estimation Using Free Response Measured by a Continuously Scanning Laser Doppler Vibrometer System With Application to Structural Damage Identification," J. Sound. Vib., **485**.
[26] Presas, A., Valentin, D., Egusquiza, E., Valero, C., Seidel, U., and Weber, W., 2016, "Natural Frequencies of Rotating Disk-Like Structures Submerged Viewed From the Stationary Frame," IOP Conf. Ser. Earth Environ. Sci.
[27] Stanbridge, A. B., Martarelli, M., and Ewins, D. J., 2001, "Rotating Disc Vibration Analysis With a Circular-Scanning LDV," Proceedings of the International Modal Analysis Conference—IMAC XIX, Kissimmee, FL, Feb. 5–8, pp. 464–469
[28] Stanbridge, A. B., Sever, I. A., and Ewins, D. J., 2002, "Vibration Measurements in a Rotating Blisk Test Rig Using an LDV," Fifth International Conference on Vibration Measurements by Laser Techniques: Advances and Applications, Ancona, Italy, June 22–25.
[29] Halkon, B. J., and Rothberg, S. J., 2006, "Vibration Measurements Using Continuous Scanning Laser Vibrometry: Advanced Aspects in Rotor Applications," Mech. Syst. Signal. Process., **20**(6), pp. 1286–1299.
[30] Gasparoni, A., Allen, M. S., Yang, S., Sracic, M. W., Castellini, P., and Tomasini, E. P., 2010, "Experimental Modal Analysis on a Rotating Fan Using Tracking-CSLDV," 9th International Conference on Vibration Measurements by Laser and Non-Contact Techniques and Short Course, Ancona, Italy, June 22–25, pp. 2–16.
[31] Castellini, P., and Santolini, C., 1998, "Vibration Measurements on Blades of a Naval Propeller Rotating in Water With Tracking Laser Vibrometer," Measurement, **24**(1), pp. 43–54.
[32] Abbas, S. H., Jang, J. K., Kim, D. H., and Lee, J. R., 2020, "Underwater Vibration Analysis Method for Rotating Propeller Blades Using Laser Doppler Vibrometer," Opt. Lasers Eng., **132**, p. 106133.
[33] Kubota, Y., and Suzuki, T., 1984, "Added Mass Effect on Disc Vibrating in Fluid," Trans. Jpn. Soc. Mech. Eng. C, **50**(449), pp. 243–248.
[34] Presas, A., Valentin, D., Egusquiza, E., Valero, C., and Seidel, U., 2015, "Influence of the Rotation on the Natural Frequencies of a Submerged-Confined Disk in Water," J. Sound. Vib., **337**, pp. 161–180.
[35] Lyu, L. F., and Zhu, W. D., 2022, "Operational Modal Analysis of a Rotating Structure Subject to Random Excitation Using a Tracking Continuously Scanning Laser Doppler Vibrometer via an Improved Demodulation Method," ASME J. Vib. Acoust., **144**(1), p. 011006.
[36] Lyu, L. F., Higgins, G. D., and Zhu, W. D., 2022, "Operational Modal Analysis of a Rotating Structure Using Image-Based Tracking Continuously Scanning

Laser Doppler Vibrometry via a Novel Edge Detection Method," J. Sound. Vib., **525**.
[37] Lyu, L., and Zhu, W., 2024, "A Novel Image-Based Long-Range Continuously Scanning Laser Doppler Vibrometer for Operational Modal Analysis of a Rotating Structure," Res. Nondestruct. Eval., **35**(6), pp. 303–318.
[38] Presas, A., Valentin, D., Valero, C., Egusquiza, M., and Egusquiza, E., 2019, "Experimental Measurements of the Natural Frequencies and Mode Shapes of Rotating Disk-Blades-Disk Assemblies From the Stationary Frame," Appl. Sci., **9**(18).
[39] Di Maio, D., Magi, F., and Sever, I. A., 2018, "Damage Monitoring of Composite Components Under Vibration Fatigue Using Scanning Laser Doppler Vibrometer," Exp. Mech., **58**(3), pp. 499–514.
[40] Staszewski, W. J., Jenal, R. B., Klepka, A., Szwedo, M., and Uhl, T., 2012, "A Review of Laser Doppler Vibrometry for Structural Health Monitoring Applications," Key. Eng. Mater., **518**, pp. 1–15.
[41] Leissa, A. W., 1969, *Vibration of Plates. Washington: Scientific and Technical Information Division*, National Aeronautics and Space Administration, Washington, DC.
[42] Dätig, M., and Schlurmann, T., 2004, "Performance and Limitations of the Hilbert-Huang Transformation (HHT) With an Application to Irregular Water Waves," Ocean Eng., **31**(14–15), pp. 1783–1834.
[43] Kuttler, K. L., 2021, Elementary Linear Algebra.
[44] Moraga, G., Egusquiza, M., Valentín, D., Valero, C., and Presas, A., 2022, "Analysis of the Mode Shapes of Kaplan Runners," Appl. Sci., **12**(13).
[45] Magara, Y., Narita, M., Takahashi, N., Yamaguchi, K., Kuwano, T., and Miura, H., 2010, "Natural Frequency of Centrifuga Compressor Impeller in High Pressure Gas," Dynamics and Design Conference, Kyotanabe, Japan.
[46] Magara, Y., Narita, M., Yamaguchi, K., Takahashi, N., and Kuwano, T., 2008, "Natura Frequencies of Centrifugal Compressor Impellers for High Density Gas Applications," ASME 2008 International Mechanical Engineering Congress and Exposition, Boston, MA, Oct. 31 - Nov. 6, pp. 1077–114.
[47] Wang, D., Luo, G., and Wang, F., 2015, "Vibration Characteristics Analysis of a Centrifugal Impeller," Vibroeng. Proc., **5**, pp. 287–291.
[48] Lin, H., Bao, H., Zhang, H., Zhao, F., and Wang, J., 2024, "Strength and Vibration Analysis of Axial Flow Compressor Blades Based on the CFD-CSD Coupling Method," Appl. Sci., **14**(16).
[49] Heinemann, T., and Becker, S., 2017, "Axial Fan Blade Vibration Assessment Under Inlet Cross-Flow Conditions Using Laser Scanning Vibrometry," Appl. Sci., **7**(8).
[50] Fakhari, S. M., and Mrad, H., 2024, "Optimization of an Axial-Flow Mine Ventilation Fan Based on Effects of Design Parameters," Results Eng., **21**.
[51] Kalmár-Nagy, T., Bak, B. D., Benedek, T., and Vad, J., 2015, "Vibration and Noise of an Axial Flow Fan," Period. Polytech. Mech. Eng., **59**(3), pp. 109–113.
[52] Uslu, S., Bayraktar, M., Demir, C., and Bayraktar, S., 2021, "Innovative Computational Modal Analysis of a Marine Propeller," Appl. Ocean Res., **113**.
[53] Valero, C., Egusquiza, M., Valentin, D., Presas, A., and Moraga, G., 2022, "Determination of the Natural Frequencies of a Prototype Kaplan Turbine," IOP Conf. Ser. Earth Environ. Sci., **1079**.
[54] Moraga, G., Mut, V., Girardelo, J., Mazzouji, F., Valentín, D., Egusquiza, M., et al., 2024, "Excessive Vibrations Experienced in a Kaplan Turbine at Speed No Load," Eng. Fail. Anal., **160**, p. 108228.
[55] Zhang, M., Valentín, D., Valero, C., Egusquiza, M., and Egusquiza, E., 2019, "Failure Investigation of a Kaplan Turbine Blade," Eng. Fail. Anal., **97**, pp. 690–700.